ChemSusChem

Research Article
doi.org/10.1002/cssc.202300344

Chemistry Europe
European Chemical Societies Publishing

www.chemsuschem.org

Hydrothermal Fabrication of Carbon-Supported Oxide-Derived Copper Heterostructures: A Robust Catalyst System for Enhanced Electro-Reduction of CO_2 to C_2H_4

Venkata S. R. K. Tandava,[a, b] Maria Chiara Spadaro,[c] Jordi Arbiol,[c, d] Sebastián Murcia-López,*[a] and Joan Ramón Morante[a, e]

Anthropogenic CO_2 can be converted to alternative fuels and value-added products by electrocatalytic routes. Copper-based catalysts are found to be the star materials for obtaining longer-chain carbon compounds beyond $2e^-$ products. Herein, we report a facile hydrothermal fabrication of a highly robust electrocatalyst: in-situ grown heterostructures of plate-like CuO–Cu_2O on carbon black. Simultaneous synthesis of copper-carbon catalysts with varied amounts of copper was conducted to determine the optimum blend. It is observed that the optimum ratio and structure have aided in achieving the state of art faradaic efficiency for ethylene $>45\%$ at -1.6 V vs. RHE at industrially relevant high current densities over 160 to 200 $mA \cdot cm^{-2}$. It is understood that the in-situ modification of CuO to Cu_2O during the electrolysis is the driving force for the highly selective conversion of CO_2 to ethylene through the *CO intermediates at the onset potentials followed by C–C coupling. The excellent distribution of Cu-based platelets on the carbon structure enables rapid electron transfer and enhanced catalytic efficiency. It is inferred that choosing the right composition of the catalyst by tuning the catalyst layer over the gas diffusion electrode can substantially affect the product selectivity and promote reaching the potential industrial scale.

Introduction

The circular economy of CO_2 is a hot issue amid global warming. Nevertheless, the successful implementation of novel technologies still demands a lot of new research to orient into reliable systems. Significant research has been carried out on thermal catalysis,[1] photocatalysis,[2] photoelectrocatalysis and biocatalysis[3] for the effective mitigation of CO_2 to various chemical feedstocks. Of all these methodologies, electrocatalytic CO_2 reduction (ECO_2R) is proven to be a promising strategy to mitigate CO_2 emissions.[4] To meet the global energy demands and to curb the increasing amounts of CO_2 in the atmosphere, developing functional advanced nanostructured catalyst materials and systems for electrochemical conversion of CO_2 to alternative fuels or value-added products is the need of the hour.[5,6] The selectivity for the ECO_2R is based on the applied voltages/currents and the number of electrons transferred/exchanged depending on the catalyst material used. However, CO_2 being a linear molecule is highly stable and its low solubility in the electrolyte makes the overall process quite challenging. Issues like low product selectivity, high overpotentials and the highly competitive Hydrogen Evolution reaction (HER) are to be considered to make ECO_2R industrially viable. Owing to this demand, a wide variety of materials including metals and metal oxides,[7] single-atom catalysts,[8] MOF-derived catalysts,[9,10] and heteroatom-doped carbon-based materials[11] have been tested for the selectivity towards various value-added products like carbon monoxide (CO),[12] ethylene, ethanol[13,14] and n-propanol.[15]

Of all the various products, ethylene is the simplest C_2 product with a high market price thus remaining an attractive target for the reduction of CO_2 emissions.[16] It is formed through multiple electron-proton transfer mechanisms (12 electrons) carrying a high energy density. Although several metallic catalysts were examined, extensive research has been done by deploying copper and copper-based materials and found to be exceptionally active and effective in the selective conversion of CO_2 to greater than 2 electron products. Copper-based materials are found to possess adequate adsorption energy towards *CO intermediate[16,17] and have shown a unique ability in aiding C–C coupling to two or more carbon products. Significant studies have been made on various forms of copper including copper foils,[18] nanoparticles,[19] nanopores,[20]

[a] V. S. R. K. Tandava, Dr. S. Murcia-López, Prof. Dr. J. R. Morante
Catalonia Institute for Energy Research (IREC)
Jardins de les Dones de Negre 1, 08930, Sant Adrià de Besòs (Spain)
E-mail: smurcia@irec.cat
[b] V. S. R. K. Tandava
Universitat Autonoma de Barcelona (UAB)
Bellaterra 08193 (Spain)
[c] Dr. M. C. Spadaro, Prof. Dr. J. Arbiol
Catalan Institute of Nanoscience and Nanotechnology (ICN2), CSIC and BIST, Campus UAB
Bellaterra, Barcelona, Catalonia, 08193 (Spain)
[d] Prof. Dr. J. Arbiol
ICREA
Pg. Lluís Companys 23, 08010, Barcelona, Catalonia (Spain)
[e] Prof. Dr. J. R. Morante
Faculty of Physics
Universitat de Barcelona
Barcelona, 08028, Catalonia (Spain)

Supporting information for this article is available on the WWW under https://doi.org/10.1002/cssc.202300344

nanowires,[21] nanosheets,[22] and more recently oxide-derived species.[23]

Interestingly, oxide-derived heterostructures have shown a significant effect on CO dimerization through the C–C coupling mechanism leading to C_2H_4 selectivity.[24] Also, the addition of oxides on Cu sites has been reported to alter the adsorption behaviour of the reaction intermediates, thus tuning the reduction mechanism.[25] However, oxide-derived Cu catalysts are prone to reduce to metallic copper (Cu^0) when working under reduction potentials or currents as the ones required to drive the ECO_2R. Once they are reduced to metallic copper, it is highly likely to notice that the catalysts tend to become inactive or to decrease their ability towards C–C coupling, thereby hampering the C_2 product formation in a short span,[26] and even favouring the competitive HER. Therefore, the rational design of highly stable oxide-derived copper-based catalysts is required to achieve higher CO_2 conversions operating at industrially relevant current densities and with greater stabilities. In the recent past, a strong focus is levied on carbon-based materials as efficient electrocatalysts for the ECO_2R owing to their intrinsic properties, such as high surface areas, excellent electrical conductivity, and high mechanical strength, largely facilitating the diffusion of CO_2. Different types of carbon-based materials like pure carbon-derived catalysts,[27,28] hetero-atom-doped carbon catalysts[29] and metal-carbon single-atom catalysts[30] have been explored to achieve high catalytic efficiencies. Moreover, carbon black (C-Black) has been used as standard support in electrode formulations for electrolysis, batteries, and fuel cell applications.[31] Although several strategies have been followed including direct support of electrocatalysts on carbon black,[32,33] the physical mixture of carbon and catalyst for ink formulations is the most extended approach[26,34] leading to non-optimal catalyst-to-carbon contact.

As a result, we propose the quasi-functionalisation of C-Black through in-situ growth of oxide-derived copper heterostructures as alternative to having stronger adhesion, attaining high current densities, facilitating higher gas diffusion, and improving the catalytic efficiency with possible aid in the electron transfer mechanism.

Herein, we report a study on Cu/C-based electrocatalysts for the efficient electro-reduction of CO_2 to ethylene operating at high current densities. We present a facile hydrothermal route to design a robust electrocatalyst having C-Black supported oxide-derived copper heterostructures. Initial chemical reduction of a copper precursor followed by in-situ growth of CuO and Cu_2O heterostructures over C-Black was obtained. Different nominal Cu/C ratios were synthesised to determine the optimum blend and to attain the state-of-art conversion to ethylene at industrially relevant high current densities. As-synthesised electrocatalysts were deposited on gas diffusion electrodes (GDEs) and evaluated in a flow electrolyser. We elucidate the high conversion and selectivity towards ethylene as a factor of in-situ reduction of the derived CuO–Cu_2O heterostructures to Cu_2O, along with the blending with C-Black that helps to increase the conductivity and enhance the CO_2 distribution. It is also understood that choosing the right composition of the catalyst layer over the GDE can fetch the overall CO_2 reduction operating at high current densities for long hours and can make an industrially viable alternative.

Results and Discussion

Synthesis and structural characterisation of the catalyst materials

We have carried out the synthesis of Cu_xO/C heterostructures in a two-step manner as described in the experimental section. In the typical synthesis, C-Black was sonicated to widely disperse following the addition of copper acetate precursor. The mixture solution was heated to 60 °C before transferring to the hydrothermal autoclave which was maintained at 160 °C for 12 h. For a comparative study, we have also synthesised different combinations of Cu/C ratios by altering the copper content to understand the best blend for the in-situ growth. When compared with the physical addition of C-Black with the as-synthesised bare Cu_xO catalyst particles during the ink formulations, the direct in-situ growth of oxide-derived copper heterostructures showed a significant influence in the improved catalytic efficiency indicating the copious amounts of exposed active sites on the C-Black facilitating the rapid electron transfer mechanism. A detailed synthesis protocol with materials and methods of electrode fabrication is given in the experimental methods section.

Initial compositional and structural properties were examined using XRD analysis of the as-prepared samples: bare Cu_xO, Cu_xO/C1, Cu_xO/C2 and Cu_xO/C3 heterostructures, along with the Vulcan (C-Black). As shown in Figure 1a, the standard Cu_xO/C2 is deemed to have the CuO tenorite monoclinic phase (JCPDS 048-1548) at 35.5°, 38.7°, 38.9°, 48.7°, 53.3° and 66.2° corresponding to (−111), (111), (200), (−202), (020), (−311) planes. The peaks located at 36.4°, 42.3°, 61.4° and 73.5° correspond to (111), (200), (220) and (311) planes of Cu_2O cuprite cubic phases respectively (JCPDS 005-0667). On the other hand, samples of bare Cu_xO, Cu_xO/C1, Cu_xO/C2 and Cu_xO/C3 were analysed under the same conditions. The presence of metallic copper (JCPDS 004-0836) in the bare Cu_xO sample (prepared without any addition of C-Black) along with dominant CuO and Cu_2O phases are seen. The sample Cu_xO/C1 revealed the sole presence of CuO having low copper content, and the Cu_xO/C3 seemed to be very coherent with Cu_xO/C2 but with a higher content of Cu_2O along with CuO. Table S1 shows the quantitative comparison of CuO, Cu_2O and metallic Cu, estimated from the XRD of all the blends. As seen, CuO content in the Cu_xO/C samples decreases inversely with the initial ratio of Cu precursor to Vulcan, while the opposite occurs with the Cu_2O phase. The presence of metallic Cu is only observed in the bare Cu_xO sample, in agreement with having more reduced species (Cu, Cu_2O) in the materials with lower C-black content. This suggests that copper precursor is more easily reduced in the absence (or in the synthesis with lower content) of carbon.

FTIR-ATR analysis confirmed the presence of CuO and Cu_2O in the Cu_xO/C2 heterostructures as shown in Figure 1b. Strong

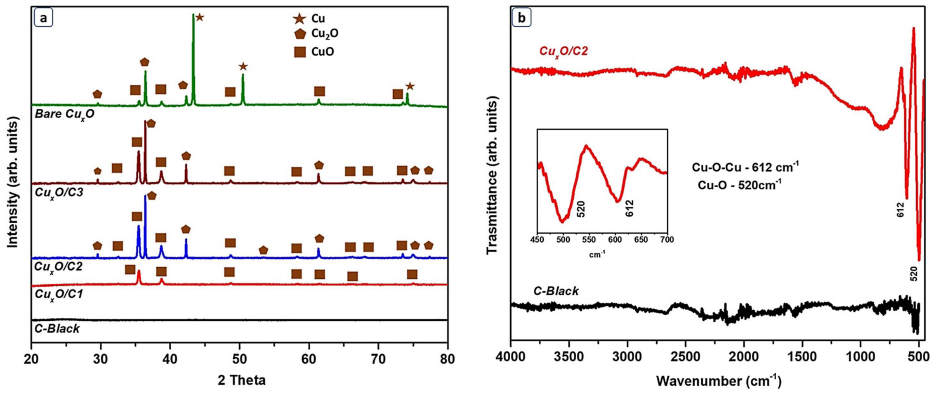

Figure 1. (a) XRD of the as-prepared Cu_xO/C heterostructures; (b) ATR-FTIR spectrum of Cu_xO/C2 and comparison with Vulcan (Inset of Cu_xO/C2 representing Cu_2O and CuO).

adsorption bands appearing at 520 cm^{-1} are attributed to the vibrations of Cu–O from CuO structures[35] and the sharp peak at 612 cm^{-1} corresponds to the vibration of Cu–O–Cu originating from Cu_2O.[36] Strong brands at 3200–3500 cm^{-1} correspond to hydroxyl groups and are observed in correlation with the C-Black band spectrum. At 1560 cm^{-1}, carboxyl functional groups are identified with higher intensity compared to the pure C-Black.

The nitrogen adsorption-desorption measurements were performed to assess any changes in the surface area of copper heterostructures as a result of the incorporated C-Black. The surface area is calculated using Brunauer-Emmett-Teller (BET) analysis and the resultant pore size distributions were analysed. The BET adsorption plots and linear isotherms with the corresponding pore size distributions shown in Figure S1a and b clearly depict a type III isotherm. The relative surface area of Cu_xO/C2 (CuO–Cu_2O/C-Black) is around 57.3 $m^2 \cdot g^{-1}$ whereas the one of the Cu_xO is only around 6.3 $m^2 \cdot g^{-1}$ showing a 9-fold increase in the relative surface area. Thus, this analysis in turn proves that the direct growth of supported copper on carbon black leads to heterostructures with higher surface area and pore volumes with respect to Cu_xO particles. This increased area and porosity might facilitate the diffusion of active species (i.e., CO_2 and ions).

X-ray photoelectron spectroscopy (XPS) was used to investigate the surface and compositions of the synthesised catalysts. A comparative study has been done on the carbon-supported Cu_xO/C2 catalyst and as prepared bare Cu_xO. The obtained XPS spectrum confirmed the presence of the elements Cu, O and C in correlation with the corresponding binding energies of Cu 2p, O 1s and C 1s orbitals. Figure 2a shows the high-resolution spectrum of the core 2p level revealing the main characteristic peaks. Upon further deconvolution of the set of two peaks representing the main Cu $2p_{3/2}$ and $2p_{1/2}$ spin orbits, the presence of Cu^+ in the Cu_2O structures was confirmed by two peaks at 933.13 and 953.01 eV. Similarly, peaks with the binding energies 934.8 and 955.2 eV and corresponding to Cu^{2+} in CuO heterostructures were found. On the other hand, the deconvolution of O 1s, Figure 2b shows the typical peaks of lattice O_2^- in Cu–O and Cu_2O at 530.18 and 531.30 eV, along with a prominent peak at 532.65 eV corresponding to the C–O–C species on the Cu/C interface. Also, the high-resolution C 1s spectrum (Figure 2c) shows the C–C bonding at 284.76 eV from C-Black. The presence of C–O and C=O species are attributed to 285.71 and 287.08 eV peaks, respectively. Similarly, we have analysed the bare Cu_xO without any C-Black added. The deconvoluted high-resolution spectrum of Cu 2p level in Figure 2d shows the presence of metallic copper in correlation with XRD. Metallic copper (Cu^0) is identified, unlike the Cu2/C, along with Cu^+ and Cu^{2+} at 933.74 and 935.02 eV respectively, indicating Cu–Cu_2O–CuO heterostructures in the absence of C-Black. Also, considering the high-resolution deconvolution of O 1s, Figure 2e indicates the presence of O_2^- in CuO and Cu_2O at 530.11 and 531.45 eV, with much lower content of C–O–C species as expected, given the absence of C-Black in this sample. Considering the C 1s spectrum Figure 2f, adventitious carbon derived from partial exposure to atmospheric conditions during the synthesis is noticed as C–C and C=O species at 284.85 and 285.74 eV, respectively. Additional XPS analyses of Cu_xO/C1 and Cu_xO/C3 samples show similar trends to the XRD results in terms of Cu oxidation states, as depicted in the Cu 2p spectra in Figure S2. In the Cu_xO/C1 sample, Cu is mostly in fully oxidized form (Cu^{2+}), while in Cu_xO/C3, an important contribution of Cu^+ is also observed.

Initial FE-SEM imaging of the as-synthesised samples in Figure 3 and Figure S3 reveal that oxide-derived Cu heterostructures were aligned over the C-Black. Interestingly, the samples with different compositions exhibited different morphologies while anchored over the C-Black, involving platelet to rod- and cuboid-like structures surrounded by carbon particles. The bare Cu_xO particles obtained in the absence of C-Black, Figure 3a and Figure S3a and b show mixed morphologies like rods, cubes, and rectangular structures with varied particle sizes. Cu_xO/C2 sample (Figure 3c and Figure S3e and f) is found to have a more uniform morphology consisting mainly of platelet-like structures along with a minor presence of rods particles, and a homogenous distribution of Cu_xO/C heterostructures. Cu_xO/C1 sample, with lower copper content (Fig-

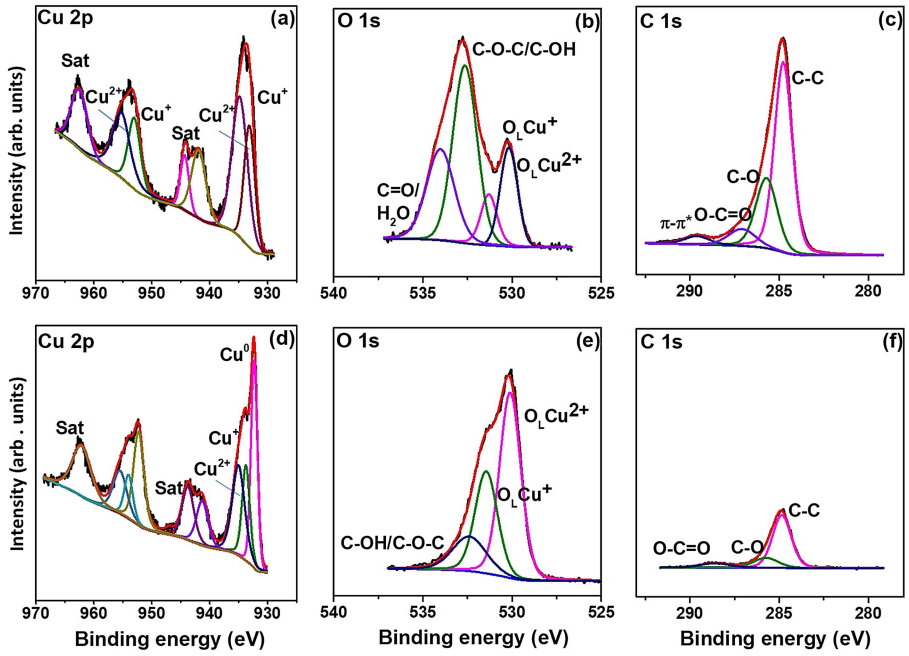

Figure 2. High-resolution deconvoluted XPS spectra of Cu_xO/C2 and comparison with bare Cu_xO (a) Cu 2p; (b) O 1s; (c) C 1s spectra of Cu2/C; (d) Cu 2p; (e) O 1s; (f) C 1s spectra of bare Cu.

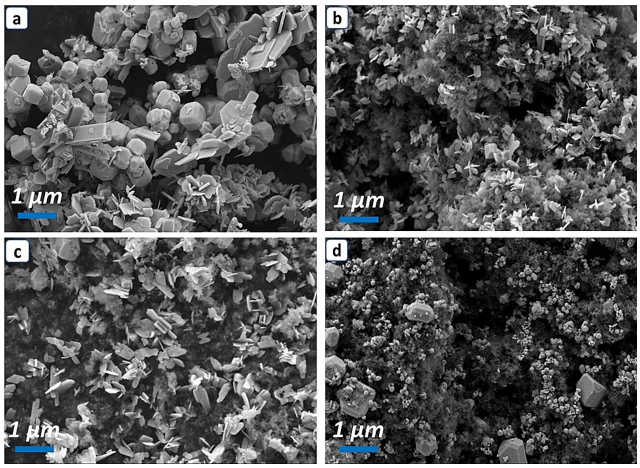

Figure 3. FE-SEM images of as-prepared samples (a) bare Cu_xO (b) Cu_xO/C1 (c) Cu_xO/C2 (d) Cu_xO/C3.

ure 3b and Figure S3c and d) has exhibited similar morphology to Cu_xO/C2 but with lesser coverage of Cu. The Cu_xO/C3 blend, with higher nominal copper content (Figure 3d and Figure S3g and h) has a drastic change in terms of morphology showing cubic and large octahedral crystals with heterogeneous particle size. The EDX analysis of the different compositions in Figure S4a–c revealed the presence of Cu, C and O with Cu averaging around 25–40%, O around 10% and the rest by carbon. A comparison of elemental composition along with EDX analysis is given in Table S3 along with the nominal Cu/C ratios. Interestingly, despite the higher nominal amount of Cu precursor on the Cu_xO/C3 sample, the Cu content on Cu_xO/C2 and Cu_xO/C3 is similar and lower than the theoretical one as per the amount of Cu precursor. In fact, both samples depict similar Cu/C atomic ratios of 0.1, which ultimately implies that the differences in the performance between both materials are not associated with different Cu content.

The presence of partial oxidized copper species surrounded by cloud-like carbon structures is evident from transmission electron microscopy (TEM) (as shown in Figure 4a and b) images. Low magnification TEM confirmed the presence of Cu-based heterostructures surrounded by C-based clouds. HAADF-STEM images in Figure 4c and d clearly show Cu heterostructures with dominating platelet-like morphologies, which present various faceting. The power spectra (fast Fourier transforms) calculated on the HRTEM images obtained on the C-based "cloud-like" structures (see Figure 4e and f) show that they present a periodicity corresponding to an interplanar distance of about 0.34 nm, in perfect agreement with a graphitic-like crystal structure. The C-based structures are evidenced in red in the frequency-filtered map reported in Figure 4f. These carbon nanostructures resemble graphitic onion-like rings.

The HRTEM analyses performed on the Cu-based nanoplatelets suggest that their structure corresponds to the monoclinic tenorite CuO crystal phase, in complete good agreement with our initial XRD studies. The observed CuO structures imaged in Figure 5a and b are oriented along the [011] and [101] zone axes parallel to the electron beam. Electron energy loss spectroscopy (STEM-EELS) (Figure 5c and d) was used to obtain the elemental composition of the sample, focusing the attention on C K-edge at 284 eV (green), O K-edge at 532 eV (blue) and Cu L-edge at 931 eV (red). The analysis performed over the platelet-like structures revealed the homo-

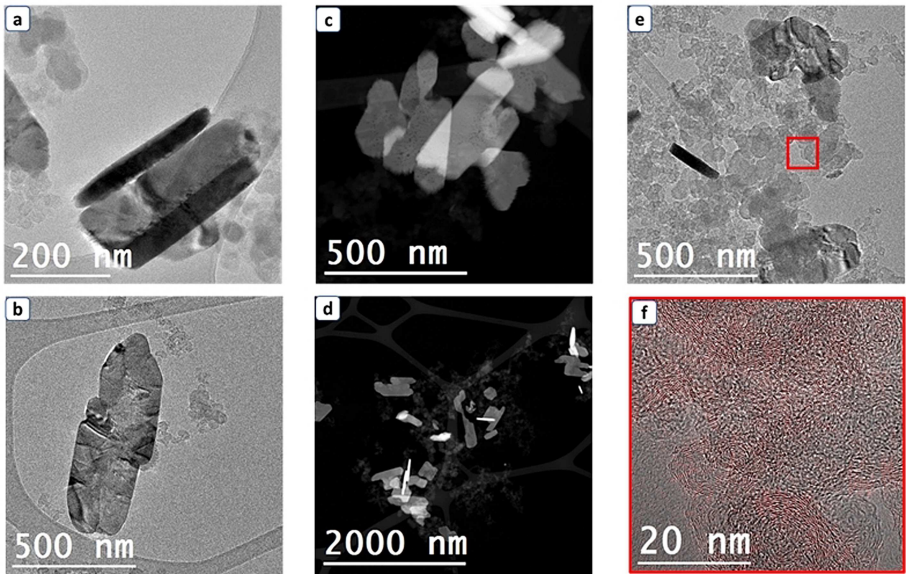

Figure 4. TEM and STEM-HAADF images of Cu_xO/C2: (a, b, e) low magnification TEM, (c, d) low magnification STEM-HAADF images, (f) high-resolution TEM combined with the frequency filtered map to evidence the graphitic structure (in red).

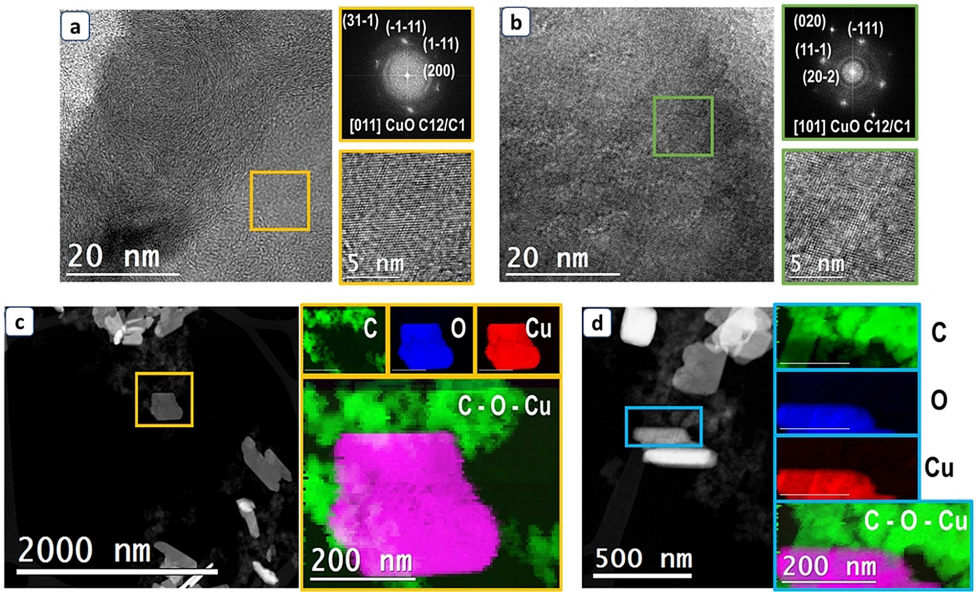

Figure 5. HR-TEM and STEM-EELS images of Cu_xO/C2: (a, b) high-resolution TEM together with the detailed image and corresponding power spectra. (c, d) STEM-HAADF and corresponding STEM-EELS compositional analysis.

genous distribution of Cu and O surrounded by carbon structures. Low magnification TEM of the bare Cu_xO also confirms the presence of Cu-based structures with sizes in the range of a few microns with varied morphologies like platelets, rods, or cubes, as shown in Figure S5a and b. These large-sized particles are highlighted using the image contrast of HAADF-STEM as shown in Figure S5c and d. Detailed investigation using the power spectrum analysis of HRTEM (Figure S5e and f) confirmed the presence of both CuO tenorite monoclinic crystal phase as on the left side, imaged along [011] and Cu_2O cuprite cubic structure as on the right side, imaged along [11-1] zone axis. STEM-EELS maps (Figure S5g) on C K-edge at 284 eV (green), O K-edge at 532 eV (blue) and Cu L-edge at 931 eV (red) indicate that the Cu and O are homogeneously distributed within the nanostructures, in good agreement with the structural analysis.

Linear sweep voltammetry and ECSA analysis

Electrochemical double-layer capacitance measurements were performed to analyze the active surface area of the synthesised

electrocatalysts. Figure S6 depicts the ECSA analysis along with double-layer capacitance C_{DL} plots. ECSA analysis was performed in a standard three-electrode cell configuration. A glassy carbon electrode with the catalyst ink deposited was used as the working electrode, a platinum mesh as the counter electrode and a Hg/Hg_2SO_4 electrode as the reference. A non-faradaic region with the applied potential range of −0.4 to −0.5 V vs. RHE was chosen, and cyclic voltammetry was performed at various scan rates in Ar-saturated 1 M $KHCO_3$ aqueous solution. The plots of scan rates ($mV \cdot s^{-1}$) vs. current (I) are shown, and the slope represents the specific double-layer capacitance C_{DL}. Cu_xO/C1 and Cu_xO/C2 are found to have C_{DL} values of 0.3 and 0.27 mF, respectively, higher than bare Cu_xO (0.11 mF), suggesting the presence of a higher number of active sites. Though the sample with higher copper nominal content, Cu_xO/C3, presents the highest capacitance (0.83 mF), the morphology and the ratio of CuO to Cu_2O seem to be the limiting factors in its selectivity towards ethylene via ECO_2R. Linear sweep voltammetry studies (in Figure S7) were performed under CO_2 and Ar-saturated electrolytes to study the behaviour of the electrocatalysts at different potentials. In general, all the Cu-based samples exhibit lower onset potentials than C-Black. Although minor differences were observed in the LSV curves under CO_2 and Ar flows, Cu_xO/C2 displays slightly higher cathodic currents in the presence of CO_2, thus confirming its intrinsic higher activity towards ECO_2R. On the contrary, both Cu_xO/C3 and bare Cu_xO show high currents with Ar at more cathodic potentials. More intense reduction peaks are observed in all the samples at less negative potentials (0 to −0.2 V_{RHE}) in the measurements under Ar flow, suggesting a lower tendency of Cu_xO species to be reduced in the presence of CO_2.

Electrochemical reduction of CO_2 in a flow electrolyser

We have performed the electrochemical reduction of CO_2 by deploying the synthesised Cu_xO/C heterostructures in an electrochemical flow cell in a three-electrode configuration as shown in Figure 6. We have assessed all the synthesised catalysts and made a comparative study to find the best blend and morphology. Two approaches to the gas-electrolyte configuration have been carried out: flow-by and flow-through operational modes. Electrolysis was performed via chronoamperometric measurements for at least 60 min at each applied potential ranging between −1.1 and −1.5 V vs. RHE. Gaseous products were analysed and quantified using an online GC. The electrolysis was performed for 60 min with periodic injections to quantify the gas products.

The performed ECO_2R fetched the potential-dependent selectivity of the main products as ethylene, carbon monoxide, hydrogen and trace amounts of methane and ethane. The oxide-derived copper heterostructures are highly selective towards ethylene as observed during the gradual sweep towards increasing cathodic potentials. All different compositions were evaluated and compared, and the faradaic efficiencies of various catalysts for major gas products at different applied potentials are plotted in Figure 7. The respective gas chromatograms of the analysed sample along with the calibration chromatogram are shown in Figure S8 indicating C_2H_4, CO and H_2 as the major products while negligible amounts of CH_4 and C_2H_6 were noticed (< 0.5 % FE). The observed current densities were also represented in Figure 7d for all the samples measured. Figure S9 gives a detailed representation of corresponding faradaic efficiencies and current densities for each analysed sample. Figure S9d comparatively shows the efficiencies with the different materials at the best operation conditions for ethylene generation along with the obtained current densities. Comparatively, enhanced selectivity towards C_2H_4 is seen with the Cu_xO/C2 sample, while the other samples led to much lower FE C_2H_4 values. At low potential values (−1.1 to −1.3 V vs. RHE), Cu_xO/C1 exhibited only slightly lower efficiencies than Cu_xO/C2, although the values rapidly dropped after further increasing the polarisation values, with a concomitant increase in the H_2 generation. This composition (Cu_xO/C1) resulted in an initial faradaic efficiency of 41 % towards CO, but the lower number of available active sites (low Cu/C ratio) turned the catalyst layer inactive towards carbon products within a short time. Similarly, the material with higher nominal copper content, Cu_xO/C3, which is seen to have a completely different morphology and higher initial Cu_2O compared to Cu_xO/C2, shows higher overpotential towards C_2H_4 formation, with the FE C_2H_4 linearly increasing with working potential, while efficiency to CO is kept relatively constant between 20–

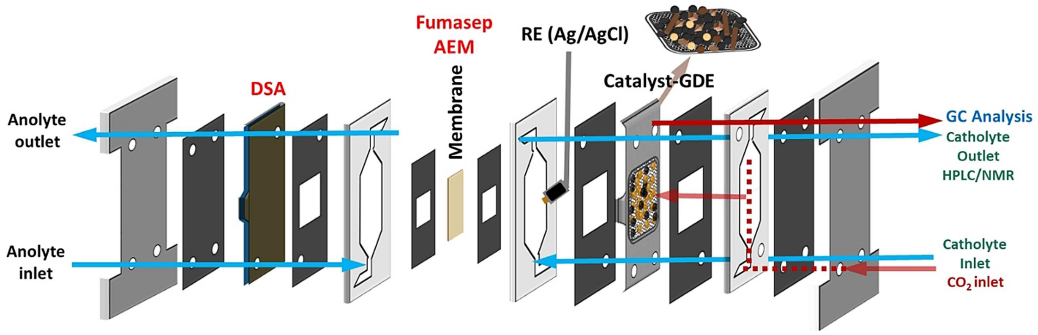

Figure 6. Experimental setup of flow electrolyser for ECO_2R.

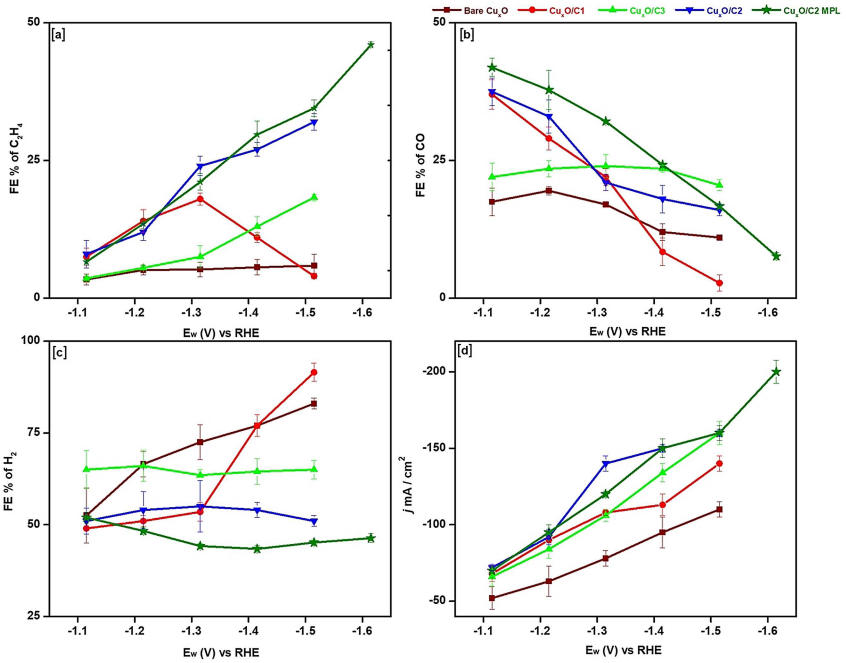

Figure 7. Electrocatalytic performance of CO_2 reduction of different samples. Faradaic efficiencies (FE%) of (a) C_2H_4, (b) CO, and (c) H_2; (d) current densities at different potentials.

25%. Therefore, despite the higher nominal Cu-content and the higher ECSA value in Cu_xO/C3, it is inferred that the morphology and crystalline structure are not favouring the higher selectivity towards C_2H_4 over H_2. It is understood that, even at higher applied potentials and currents, the morphology, and the ratio of initial oxide states of copper of the synthesised heterostructures play a crucial role in tuning the selectivity towards the desired ethylene. We have also analysed bare Cu_xO along with the addition of C-Black (Vulcan) to understand the efficiency of the synthesis and to see if the in-situ growth of CuO over C-Black is advantageous over the addition of physical mixture during the catalyst ink formulations. It is noted that these catalysts are poorly selective towards C_2H_4 and only competitive HER is favoured, with faradaic efficiencies to H_2 higher than 75%. A table representing the productivity differences between bare Cu_xO and Cu_xO/C2 has been given in Table S2.

In general, flow-by mode has been considered to be more suitable for industrial applications than flow-through configuration, based on certain advantages such as lower ohmic drops and higher stability attained by controlled perspiration (provided flooding is avoided) and decreased salt formation.[37] Therefore, an additional test was performed with the Cu_xO/C2 material by preparing an electrode on commercial carbon Toray with microporous layer (MPL) and using flow-by conditions. In Figure 8, we show the performance of the prepared Cu_xO/C2 blend along with flow-through and flow-by analyses. At −1.5 V, a slightly higher faradaic efficiency towards ethylene (FE C_2H_4) was achieved (36%) at a current density of 160 mA·cm^{-2}. When a current density of 200 mA·cm^{-2} was continuously applied in flow-by mode, an exponential surge of FE C_2H_4 to 46% was

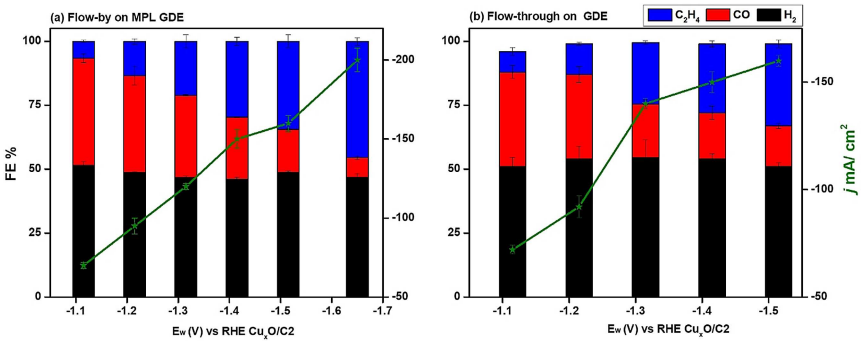

Figure 8. Electrocatalytic performance of CO_2 reduction via flow-by (a) and flow-through (b) operation modes.

achieved, while limiting the one of H_2 to around 40%. Although slightly enhanced values are observed in the flow-by test, intrinsic differences associated to the presence of MPL precludes exhaustive comparison.

At the end of the electrolysis, the liquid products were analysed by taking a fraction of the catholyte and using GC with a head space accessory with an auto-sampler. Trace amounts of methanol (96 ppm), ethanol (1350 ppm) and n-propanol (390 ppm) were formed and accumulated in the catholyte, which accounts for insignificant FE values. A chromatogram representing the major liquid products is shown in Figure S10. An additional stability test was performed at the standard operating galvanostatic conditions in the flow-by mode with a constant applied current of 160 $mA \cdot cm^{-2}$ yielding a faradaic efficiency of over 38% holding excellent stability of more than 12 hours. Figure S11 shows the stability performance in the aforementioned conditions. Figure S12 provides a comparative analysis of the electrocatalytic performance of CO_2 reduction of FE% of CO and C_2H_4 of different compositions prepared and analysed concerning the applied potentials. With Cu_xO/C electrocatalysts, CO is the favoured product noticed at lower polarisation values, while a selectivity shift towards C_2H_4 is observed with gradual cathodic sweep, indicating the unique ability of the synthesised electrocatalysts to promote dimerization reactions. Unlike this, the C_2 selectivity with bare Cu_xO sample does not significantly change with the applied potential, and H_2 remains to be the majoritarian product.

XRD post-electrolysis measurements in Figure S13a confirm that CuO is reduced to Cu_2O in all the compared samples. Figure S13b depicts the change in the Cu phases of Cu_xO/C2 during the stages of electrolysis showing that the complete in-situ modification of CuO to Cu_2O phase takes place rapidly even after preliminary polarisation at low voltages. It can be further understood that the as-seen reduction to Cu_2O is the driving factor for the selectivity along with the optimum Cu/C ratio of active sites. Figure S14 shows the FE-SEM morphological comparison of the Cu_xO/C2 deposited on carbon paper: (a) as deposited on the GDE, (b) after an initial pre-reduction step and (c) post-electrolysis. The morphology depicts platelet-like structures on the as-deposited electrodes changing to small cube-like particles after the pre-reduction and in whole after the CO_2 electrolysis. The post-electrolysis TEM and HR-TEM analysis of the electrocatalysts in Figure S15 (obtained from carefully scratching the GDE surface) revealed the morphological changes to cubic and rectangular-shaped particle agglomerates as a result of the applied cathodic potentials. Modifications are seen in both structures and morphologies as mentioned above. Figure S15 depicts the low magnification TEM images of Cu-based nanostructures possessing an average size in the range of 100 mm and the HAADF-STEM studies; Figure S15c and d clearly distinguishes the C-based graphitic onion rings from the agglomerated Cu-based nanostructures. Further detailed investigation with the HR-TEM in Figure S15e and f led to the identification of corresponding structural analysis of the Cu-based nanostructures. Power spectrum analysis evaluated that all the Cu-based nanostructures possessing Cu_2O Cuprite-based cubic structures are imaged with the [001] zone axis parallel to the electron beam. To gain further insights into the elemental distribution, STEM-EELS mapping was carried out (Figure S15g and h) focusing the attention on C K-edge at 284 eV (green), O K-edge at 532 eV (blue) and Cu L-edge at 931 eV (red). A good agreement with the structural analysis is observed as the Cu and O are homogeneously distributed within the nanostructures. It is understood that the C-based nanostructures are in good contact with the Cu_2O nanoparticles. This summarises the whole mechanism involving the reduction of the CuO heterostructures to Cu_2O nanoparticles, thereby acting as the catalytic active sites for the reduction of CO_2. The post-electrolysis characterisation of the catalysts indicates the presence of Cu_2O (Cu^+) as the final state of copper. However, in-situ minor formation of Cu^0 during the electrolysis is not completely excluded, with the possibility of further re-oxidation prior to ex-situ analysis.

From the obtained results and the characterisation studies, the derived Cu_2O is found to be the main catalytic active site for the highly selective conversion of CO_2 to C_2H_4 at high current densities. Cu_2O is partially formed during the synthesis of the materials but is also derived from the electrochemical pre-reduction of CuO occurring under the initial steps. In fact, LSV studies show slightly unfavourable $Cu^{2+}/Cu^+/Cu^0$ reduction steps in presence of CO_2, in comparison to Ar atmosphere, suggesting a certain stabilisation of oxidised forms. Besides the crystallographic related aspects, mechanistic considerations already described in the literature regarding C_2H_4 formation and its correlation with the initial generation of CO* intermediate, indicate that CO* needs to be formed and adsorbed on the electrocatalyst surface in order to dimerise through a C–C coupling mechanism.[17] As seen at low polarisation values, mostly CO is formed with Cu_xO/C1 and Cu_xO/C2, which seem to have adequate adsorption energies to promote CO* formation (and further desorption as CO product). This agrees with the fact of initially observing mostly plate-like morphology on both samples. At higher polarisation, C_2H_4 generation is promoted with Cu_xO/C2 at the expense of a concomitant decrease in CO formation, thus suggesting a correlation between the two products. In the case of Cu_xO/C1, the lower Cu content seems to be the reason for the poor selectivity towards C_2H_4 at high polarisation values, although the comparison between Cu_xO/C2 and Cu_xO/C3, with similar Cu/C ratios (as seen by EDX analysis), demonstrates that the differences are not only related to the Cu content. Moreover, even while having higher ECSA (and achieving slightly higher current densities), Cu_xO/C3 depicts a different behaviour with FE to CO being constant along all the polarisation conditions, and the one of C_2H_4 increasing linearly with the applied potential (although much lower than those of Cu_xO/C2). These results clearly suggest that the polymorphic nature of Cu_xO/C3 has a detrimental effect on the ECO_2R. The effect of C-black is not only in enhancing CO_2 diffusion but also in attaining higher current densities. In fact, the evaluation of bare Cu_xO (in physical mixture with C-black), reaching significantly lower currents than the Cu_x/C materials, shreds of evidence that Cu_xO/C interaction obtained by the in-situ synthetic methods is necessary to achieve higher operating current.

Related synthetic approaches have been followed in other studies for the in-situ preparation of CuO/C structures including carbon black and other carbonaceous materials. For instance, Yang et al. prepared CuO-supported catalysts, demonstrating improved FE to C_2H_4 in correlation with CO_2 uptake capacity attained with N-doped carbon materials.[33] Although evaluated under different conditions, comparatively, the CuO material supported on XC-72 Vulcan, reached FE to C_2H_4 of 20% at current densities of 140 $mA \cdot mg_{Cu}^{-1}$, while in the present work we achieve 46% with estimated current of 133 $mA \cdot mg_{Cu}^{-1}$. In a different approach, Wang et al. have developed CuO_x/C materials with mixed oxidation states based on a chlorine induced transformation, achieving FE to C_2H_4 of 22% at 60 $mA \cdot cm^{-2}$, and demonstrating stabilisation of mixed Cu^0/Cu^+ valence states for long operation times in H-cell.[28] In general, this strategy has been demonstrated to be an effective alternative to obtain electrocatalysts with state-of-the-art activities for C_{2+} products, with scalable and relatively simple synthesis methods, while also deploying catalysts with low metal content with respect to other approaches with pure Cu-derived materials. Differently from those studies, we have developed in the present work systems with larger area electrodes, implemented in flow-cell devices with optimised flow configuration, thus attaining higher efficiencies and productivities.

Conclusions

Here, we demonstrated an easy and scalable method to produce in-situ growth of oxide-derived copper-based heterostructures over C-Black as a highly robust electrocatalyst for the effective conversion of CO_2 to ethylene. At the interface of CuO–Cu_2O/C-Black deposited over the gas diffusion electrode (GDE), we attained a faradaic efficiency of 46% at a current density of 200 $mA \cdot cm^{-2}$ in an aqueous flow electrolyser in neutral media and room temperature electrolysis. GDE-based cathodes exhibited a stable performance for a minimum of 12 hours when sweeping through increasing cathodic potentials after an initial pre-reduction at −0.5 V vs. RHE. Structural and compositional characterisation revealed that nominal Cu/C ratios were determinant in the final structural and morphological properties of the heterostructures. In the blending with optimum performance, we have confirmed the presence of initial dominating CuO phases with platelet-like morphologies having homogenous distribution over the C-Black. The effective reduction of CuO to Cu_2O indicates the initial self-evolution of the catalysts at low polarisation conditions. The presence of C-Black had a cumulative effect in not only enabling the high local CO_2 diffusion but also high current densities, while having impact in the formation of more oxidized Cu phases with more homogeneous morphologies during the synthetic procedure. This work helps in understanding the concept of carbon-supported metal oxide heterostructures synthesised by a facile hydrothermal route as robust and highly efficient electrocatalysts achieving high conversion and selectivity towards ethylene operating at high current densities thus paving the way for developing industrially viable alternatives to produce high value-added products.

Experimental Section

Materials

Vulcan XC-72 from Cabot Corp, copper (II) acetate monohydrate, NaOH from Alfa Aesar, cetyltrimethylammonium bromide (CTAB), $NaBH_4$ and $KHCO_3$, Nafion, 2-propanol were obtained from Sigma-Aldrich. All the chemicals were of analytical grade and used directly without any further purification. Toray Carbon Paper with and without MPL was purchased from The Fuel Cell Store and used directly without any modification.

Synthesis of CuO–Cu_2O/C-Black heterostructures

Inspired by a previous report of Z. Zhang et al.,[38] a modified approach was applied to obtain oxide-derived Cu/C-Black heterostructures. The schematic illustration of the synthesis protocol is shown in Figure S16. As depicted, 40 mg of commercial Vulcan XC-72 (C-Black) were dispersed in 30 mL of Milli-Q water by strong ultrasonication for 2 h resulting in a uniformly well-dispersed homogenous mixture 1. In another beaker, solution 2 was prepared by adding 200 mg of $Cu(CH_3COO)_2$ into 5 mL of MilliQ water and stirring vigorously for over 30 min. 20 mg of NaOH and 20 mg of CTAB were added to solution 2. Both the solutions (1 and 2) were further mixed and $NaBH_4$ was added to the above mix. The final suspension was further stirred for 30 min in a hot water bath maintained at 60 °C. The contents were finally transferred to a Teflon-lined stainless-steel autoclave. The oven was programmed to operate at 160 °C for 12 h and allowed to cool naturally to room temperature. The final product suspension named Cu2/C was cleaned by centrifugation with water followed by ethanol and vacuum dried at 60 °C for 24 h. A similar method is followed for bare Cu_xO without having mixture 1. By keeping the amount of C-Black (40 mg) constant, the quantity of Cu precursor was varied in order to obtain samples with different Cu_xO/C ratios: Cu_xO/C1 (100 mg of Cu precursor), Cu_xO/C2 (200 mg of Cu precursor) and Cu_xO/C3 (300 mg of Cu precursor).

Physico-chemical characterisation

Structural evaluation of the synthesised heterostructures was recorded on a Bruker type X-Ray D8 diffractometer (Cu Kα radiation, $\lambda = 1.5418$ Å, 40 kV, 40 mA) with a scanning range of 2 theta from 10° to 80° and step size of 0.025°/2 s. Morphology studies were done using a Scanning electron microscope (FE-SEM, Zeiss Auriga 60) and the composition of the synthesised heterostructures was studied by energy-dispersive X-ray spectroscopy (EDX, Oxford Inca Energy). Further investigations were carried out using high-resolution transmission electron microscopy (HR-TEM) using a field emission gun FEI Tecnai F20 microscope. High-angle annular darkfield (HAADF) scanning TEM (STEM) and electron energy loss spectroscopy (EELS) were performed in the Tecnai microscope using a GATAN QUANTUM filter for in-depth morphological and compositional analysis. X-ray photoelectron spectroscopic (XPS) studies were performed to examine the surface structural composition of the as-prepared catalyst heterostructures using a PHI instrument model 5773 Multitechnique with A1 Kα radiation (1486.6 eV). FTIR studies were performed using a Bruker FTIR-ATR. The relative surface area was studied using N_2 nitrogen adsorption-desorption measurements by Brunauer-Emmett-Teller (BET) method using TriStar II 3020-Micromeritics equipment at liquid nitrogen

temperature. Initially, the samples were degassed at 90 °C for 1 h and then at 250 °C overnight in a FlowPrep 060-Micromeritics. The BET method was used to calculate the active surface area for a relative pressure (P/P_0) range of 0.05–0.025.

Electrode fabrication

Catalyst inks were prepared by adding 20 mg of catalyst to 2 mL of 2-propanol and 100 µL of 5 wt.% Nafion. The mixtures were sonicated over an hour and directly deposited via drop-casting on the GDEs (Toray Carbon Paper 060 with and without MPL) covering the whole surface with uniform loading of the catalyst ink. All the electrodes prepared have a geometric area of 2×2.5 cm^2 exposed to the electrolyte and CO_2 interaction. The final loading of the electrocatalyst on the electrode, Toray Carbon paper is measured by weighing the electrode before and after the drop-casting of the catalyst ink. The final loading of the catalyst (Cu/C) on the GDE is found to be around 2.5 ± 0.2 mg·cm^{-2}. A commercial DSA (dimensionally stable anode) was directly used as the anode.

CO_2 electrolyser

A commercial electrochemical flow filter-press cell (Micro Flow Cell, Electrocell A/S), which was previously modified and reported in our works by Urbain et al.[12] was deployed as the CO_2 electrolyser. The schematic representation is shown in Figure 6. The cell is accompanied by a titanium plate holding the GDE cathode coupled with a commercial DSA. A leak-free Ag/AgCl (3.5 M KCl) reference electrode is mounted between the cathode and membrane chambers. An anionic exchange membrane (Fumasep FAB-PK-130) separates the cathode and anode compartments. Titanium current collector and DSA act as the electrical contact with the Bio-Logic SP50 Potentiostat. The active exposed area of the cathode is limited to 2×2.5 cm^2 and the components are separated by EPDM (ethylene propylene diene monomer) gaskets. A constant flow of CO_2, optimised to 10 mL·min^{-1} after studying the efficiency of the system at various flow rates is supplied to the electrolyser. Aqueous 1 M $KHCO_3$ (pH = 8.4) solution is the common electrolyte used in all the measurements. Catholyte and anolyte are continuously recirculated at a constant flow of 20 mL·min^{-1} connected through Tygon tubing using a peristaltic pump.

Electrolysis and product quantification

An electrochemical filter-press cell as shown in Figure 8 was used to perform the electrolysis of CO_2. Bio-Logic SP-50 Potentiostat along with a power source was used for the electrochemical measurements. For every fresh electrode, a pre-reduction at −0.5 V vs. RHE was carried out for 10 minutes before the actual electrolysis. Electrolysis was performed over a potential ranging from −1.1 V to −1.5 V for at least one hour of polarisation at each applied potential. Using Equation (1), all potentials are corrected concerning the reversible hydrogen electrode (RHE) scale,

$$E\ (\text{vs. RHE}) = E\ (\text{vs. Ag/AgCl}) + 0.209\ \text{V} + 0.059 \cdot \text{pH} \quad (1)$$

At each potential, the electrolysis was carried out for an hour and after knowing the electrolyser reached the steady state, the product gas stream was directly connected to the in-line gas chromatography (GC) equipment (Shimadzu) followed by micro-GC (Varian 490) with TCD and FID detectors to quantify all the gas products at 30-minute intervals. Current at the given potentials are obtained by considering an average value over time.

The electrolyte pH was recorded before and after the electrolysis. During the electrolysis, as mentioned above the product stream is directly connected to the inlet of the GC and automatically injected to quantify the products. The Shimadzu GC is equipped with both the flame ionization detector (FID) and thermal conductivity detectors (TCD) with an HP-PLOT column and He as the carrier gas. Catholyte and anolyte were collected at the end of electrolysis and measured using the head space GC equipped with an autosampler. As the liquid products obtained were negligible (less than 0.05 % of FE), we propose these Cu-based heterostructures are prime selective towards gas products.

The Faradaic Efficiency (FE) for each specific product is calculated using the following Equation (2)

$$\text{FE}\ [\%] = \left(\frac{M \cdot v \cdot n \cdot F}{J_{\text{total}}}\right) \times 100\,\% \quad (2)$$

Where M is the number of moles of the specific product; v is the CO_2 flow; n is the number of electrons required/exchanged to form each product (12 e^- for ethylene); F is the Faraday's constant; J_{total} is the total current at each potential.

Flow-by and flow through operation mode of CO_2 electrolyser

The CO_2 electrolyser was operated in two different modes. Initially, a flow-through mode was employed where the CO_2 gas is forced to pass through the GDE matrix, and the outlet gas is mixed with the catholyte (Figure S17b). Additionally, flow-by configuration was also evaluated (Figure S17a), with CO_2 entering the cell from the top inlet to the gas compartment and flowing by the GDE. In this mode, the diffused CO_2 passes through the MPL of GDE interacting at the liquid-solid (electrolyte-catalyst) interface and thus leaves the system together with the gas products at the bottom of the cell without mixing with the catholyte.

Acknowledgements

V.S.R.K.T. has received funding from the European Union's Horizon 2020 research and innovation programme under the Marie Skłodowska-Curie grant agreement No 754397. This work has been done in the framework of the doctorate programme in Materials Science of the Autonomous University of Barcelona. We thank Dr. M. Biset-Peiró and Dr. N.M. Carretero for their contributions to this work. IREC and ICN2 acknowledge Generalitat de Catalunya for financial support through the CERCA Program. The authors thank the support from NANOGEN (PID2020-116093RB-C43) and CERES projects (PID2020-116093RB-C42), funded by MCIN/AEI/10.13039/501100011033/ and by "ERDF A way of making Europe", by the "European Union". ICN2 acknowledges funding from Generalitat de Catalunya 2017 SGR 327. This study was also supported by MCIN with funding from European Union NextGenerationEU (PRTR-C17.I1). ICN2 is supported by the Severo Ochoa program from Spanish MCIN/AEI (Grant No.: CEX2021-001214-S).

Conflict of Interests

The authors declare no conflict of interest.

Data Availability Statement

The data that support the findings of this study are available from the corresponding author upon reasonable request.

Keywords: electrocatalytic CO_2 reduction · oxide-derived copper · gas diffusion electrodes · in-situ modification · ethylene

[1] M. D. Porosoff, B. Yan, J. G. Chen, *Energy Environ. Sci.* **2016**, *9*, 62–73.
[2] G. Sahara, O. Ishitani, *Inorg. Chem.* **2015**, *54*, 5096–5104.
[3] N. S. Weliwatte, S. D. Minteer, *Joule* **2021**, *5*, 2564–2592.
[4] M. G. Kibria, J. P. Edwards, C. M. Gabardo, C. Dinh, A. Seifitokaldani, D. Sinton, E. H. Sargent, *Adv. Mater.* **2019**, *31*, 1807166.
[5] J. Rogelj, G. Luderer, R. C. Pietzcker, E. Kriegler, M. Schaeffer, V. Krey, K. Riahi, *Nat. Clim. Change* **2015**, *5*, 519–527.
[6] S. Fuss, J. G. Canadell, G. P. Peters, M. Tavoni, R. M. Andrew, P. Ciais, R. B. Jackson, C. D. Jones, F. Kraxner, N. Nakicenovic, C. le Quéré, M. R. Raupach, A. Sharifi, P. Smith, Y. Yamagata, *Nat. Clim. Change* **2014**, *4*, 850–853.
[7] D. Ren, B. S.-H. Ang, B. S. Yeo, *ACS Catal.* **2016**, *6*, 8239–8247.
[8] J. Liu, Y. Cai, R. Song, S. Ding, Z. Lyu, Y.-C. Chang, H. Tian, X. Zhang, D. Du, W. Zhu, Y. Zhou, Y. Lin, *Mater. Today* **2021**, *48*, 95–114.
[9] Z. H. Xhao, H. L. Zhu, J. R. Huang, P. Q. Liao, X. M. Chen, *ACS Catal.* **2022**, *12*, 7986–7993.
[10] H. L. Zhu, H. Y. Chen, Y. X. Han, Z. H. Zhao, P. Q. Liao, X. M. Chen, *J. Am. Chem. Soc.* **2022**, *144*, 13319–13326.
[11] H. Cui, Y. Guo, L. Guo, L. Wang, Z. Zhou, Z. Peng, *J. Mater. Chem. A* **2018**, *6*, 18782–18793.
[12] F. Urbain, P. Tang, N. M. Carretero, T. Andreu, J. Arbiol, J. R. Morante, *ACS Appl. Mater. Interfaces* **2018**, *10*, 43650–43660.
[13] S. Ma, M. Sadakiyo, R. Luo, M. Heima, M. Yamauchi, P. J. A. Kenis, *J. Power Sources* **2016**, *301*, 219–228.
[14] C. M. Gabardo, C. P. O'Brien, J. P. Edwards, C. McCallum, Y. Xu, C.-T. Dinh, J. Li, E. H. Sargent, D. Sinton, *Joule* **2019**, *3*, 2777–2791.
[15] G. Wu, Y. Song, Q. Zheng, C. Long, T. Fan, Z. Yang, X. Huang, Q. Li, Y. Sun, L. Zuo, S. Lei, Z. Tang, *Adv. Energy Mater.* **2022**, *12*, 2202054.
[16] Y. Hori, *Electrochemical CO_2 Reduction on Metal Electrodes. In: Modern Aspects of Electrochemistry*, 42, Springer, New York, NY **2008**, p. 89–189.
[17] S. Nitopi, E. Bertheussen, S. B. Scott, X. Liu, A. K. Engstfeld, S. Horch, B. Seger, I. E. L. Stephens, K. Chan, C. Hahn, J. K. Nørskov, T. F. Jaramillo, I. Chorkendorff, *Chem. Rev.* **2019**, *119*, 7610–7672.
[18] S. Asperti, R. Hendrikx, Y. Gonzalez-Garcia, R. Kortlever, *ChemCatChem* **2022**, *14*, e202200540.
[19] I. Merino-Garcia, J. Albo, A. Irabien, *Nanotechnology* **2018**, *29*, 014001.
[20] Y. Peng, T. Wu, L. Sun, J. M. V. Nsanzimana, A. C. Fisher, X. Wang, *ACS Appl. Mater. Interfaces* **2017**, *9*, 32782–32789.
[21] M. Ma, K. Djanashvili, W. A. Smith, *Angew. Chem. Int. Ed.* **2016**, *55*, 6680–6684.
[22] B. Zhang, J. Zhang, M. Hua, Q. Wan, Z. Su, X. Tan, L. Liu, F. Zhang, G. Chen, D. Tan, X. Cheng, B. Han, L. Zheng, G. Mo, *J. Am. Chem. Soc.* **2020**, *142*, 13606–13613.
[23] A. H. Shah, Y. Wang, S. Hussain, M. B. Akbar, A. R. Woldu, X. Zhang, T. He, *Phys. Chem. Chem. Phys.* **2020**, *22*, 2046–2053.
[24] S. Y. Lee, H. Jung, N.-K. Kim, H.-S. Oh, B. K. Min, Y. J. Hwang, *J. Am. Chem. Soc.* **2018**, *140*, 8681–8689.
[25] X. Wei, Z. Yin, K. Lyu, Z. Li, J. Gong, G. Wang, L. Xiao, J. Lu, L. Zhuang, *ACS Catal.* **2020**, *10*, 4103–4111.
[26] J. Kim, W. Choi, J. W. Park, C. Kim, M. Kim, H. Song, *J. Am. Chem. Soc.* **2019**, *141*, 6986–6994.
[27] C. Jia, K. Dastafkan, W. Ren, W. Yang, C. Zhao, *Sustain. Energy Fuels* **2019**, *3*, 2890–2906.
[28] X. Wang, M. Miao, B. Tang, H. Duan, F. Zhu, H. Zhang, X. Zhang, W. J. Yin, Y. Fu, *Nano Res.* **2023**, DOI: 10.1007/s12274-023-5554-9.
[29] M. Zheng, P. Wang, X. Zhi, K. Yang, Y. Jiao, J. Duan, Y. Zheng, S.-Z. Qiao, *J. Am. Chem. Soc.* **2022**, *144*, 14936–14944.
[30] J. Zhang, W. Cai, F. X. Hu, H. Yang, B. Liu, *Chem. Sci.* **2012**, *12*, 6800–6819.
[31] S. Khodabakhshi, P. F. Fulvio, E. Andreoli, *Carbon* **2020**, *162*, 604–649.
[32] E. H. Dias, G. T. S. T. Da Silva, J. C. Da Cruz, C. Ribeiro, *ChemElectroChem* **2022**, *9*, e202200206.
[33] H. J. Yang, H. Yang, Y. H. Hong, P. Y. Zhang, T. Wang, L. N. Chen, F. Y. Zhang, Q. H. Wu, N. Tian, Z. Y. Zhou, S. G. Sun, *ChemSusChem* **2018**, *11*, 881–887.
[34] Y. C. Tan, K. B. Lee, H. Song, J. Oh, *Joule* **2020**, *4*, 1104–1120.
[35] L. Zheng, X. Liu, *Mater. Lett.* **2007**, *61*, 2222–2226.
[36] S. Deng, V. Tjoa, H. M. Fan, H. R. Tan, D. C. Sayle, M. Olivo, S. Mhaisalkar, J. Wei, C. H. Sow, *J. Am. Chem. Soc.* **2012**, *134*, 4905–4917.
[37] M. Duarte, B. De Mot, J. Hereijgers, T. Breugelmans, *ChemElectroChem* **2019**, *6*, 5596–5602.
[38] Z. Zhang, L. Sun, Z. Wu, Y. Liu, S. Li, *New J. Chem.* **2020**, *44*, 6420–6427.

Manuscript received: March 6, 2023
Revised manuscript received: June 7, 2023
Accepted manuscript online: June 12, 2023
Version of record online: August 1, 2023